Automated organ recognition using 3D mathematical morphology

John P. Strupp

Automation and Robotics Technology, M/S 82-32
Boeing Defense & Space Group, Kent, WA 98124

Robert M. Haralick

Department of Electrical Engineering, FT-10
University of Washington, Seattle, WA 98195

ABSTRACT

A method for fully automated organ recognition in 3D medical image volumes is investigated. A mathematical model for organ recognition is presented which exploits the fact that although the precise anatomy among patients differs, the basic shape of organs is consistent as are the spatial relationships between organs. 3D mathematical morphology procedures based on this model are developed using a description to algorithm translation method. The procedures first isolate an organ search volume based on the location of other organs and then extracts the goal organ using shape criteria encoded in structuring elements.

1 INTRODUCTION

Automated organ recognition enables increased utilization of medical images generated from imaging modalities such as X-ray Computed Tomography (CT) and Magnetic Resonance Imaging (MRI). These imaging modalities provide 2D images of planar slices through the body, allowing physicians to non-invasively examine the internal anatomy of patients. However, the images only give a cross-sectional view of the organs. In order to assess the 3D spatial extent of an organ, a series of adjacent 2D slice images must be examined. It can be difficult to follow the organ cross-sections from slice to slice and then mentally reconstruct its 3D shape.

Rendering a series of adjacent 2D slice images as a volume gives a visualization of organs in 3D. In order to generate an effective visualization, the individual organs need to be identified and assigned different opacities. As shown in Figure 1, the organs of interest can be made opaque, while the rest can be made translucent or transparent. With the opacities assigned, rendering of the volume data gives a 3D view into the body at the organs of interest, showing their full 3D shape and spatial relationship to each other. The visualization of an image volume can enhance the interpretation of the imaging study.

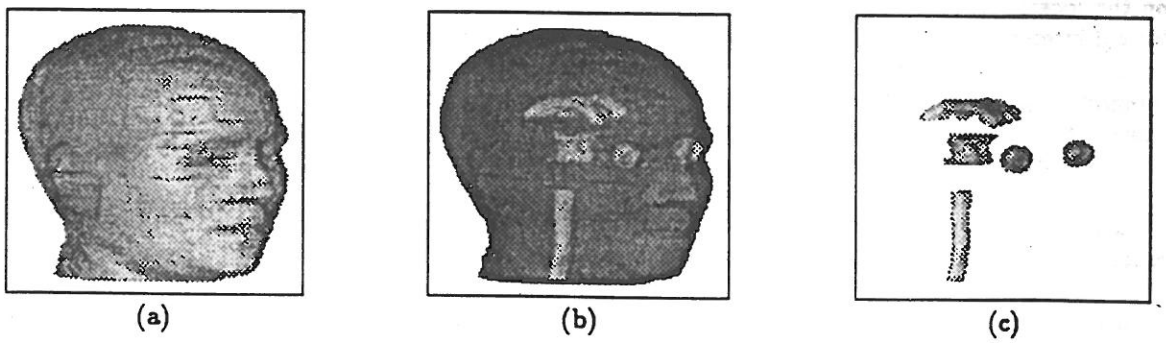

(a) (b) (c)

Figure 1: Organ Visualization.

Besides the enhanced display of the imaging data, there are many other uses for organ recognition. Application examples include radiation treatment planning, where sensitive organs, such as the eyes and optic nerves, need to be located to minimize exposure. Surgical planning could be enhanced by having the surgeon digitally practice

the procedure on the patients 3D anatomical image prior to the actual surgery. Automated organ dimensional measurements could assist in diagnosis and treatment progress assessments. The manufacture of prosthetic devices, such as a hip joint, could be customized to the individual patient. Biochemical measurements from Positron Emission Tomography (PET) or spectral MRI could be mapped to organs to assess physiological functions.

In order to create a 3D visualization of internal anatomy, the 2D slice images must be segmented into objects classes, (i.e. organs,) in order to assign opacities for the rendering process. Manually tracing organs on each slice is prohibitively time consuming for wide spread clinical use. Researchers have developed methods to semi-automate the segmentation task using the approach of providing a set of interactive tools to identify 2D contours or regions [1, 2, 3]. Although these methods are a great improvement over purely manual methods, a great deal of user effort is still required to identify several organs.

Higher levels of automation have been reported which use rule-based classification schemes to identify either the organ or tissue type of the segmented regions [4, 5, 6]. These methods calculate a set of relational, spatial and/or structural parameters for each region and then apply classification rules. The major drawback of these approaches is that the classification is done based on 2D parameters. Just as it is difficult to mentally visualize a 3D object by examining its 2D contours, the same holds true for implementing an algorithm to identify a 3D object by its 2D contours. The problem is, a 2D contour only provides partial information of the 3D nature. The location of the 2D slice needs to be known to a high degree of certainty in order to know what organs are expected to be found. This is particularly true at slice levels near the extremities of an organ. Another disadvantage of the 2D methods is that typically its extension to 3D requires manual intervention.

The proposed method is to use 3D mathematical morphology for fully automated organ recognition. The use of 3D mathematical morphology has increasingly been recognized by many researchers, in medical and industrial image processing, as an effective tool for the analysis of 3D data [7, 8, 9]. However, its use has been limited to the refinement of segmented regions, rather than being used in a comprehensive approach. It has been shown that 2D mathematical morphology can be effective in the fully automated identification of organs in image slices [10]. This work is an attempt to demonstrate the viability of extending the use of mathematical morphology to 3D organ recognition.

3D mathematical morphology organ recognition overcomes the 2D limitations by exploiting the 3D shape of organs and the spatial relationships between them for their identification. Although the precise anatomy between patients differs, the basic shape of their organs is consistent, as are the spatial relationships. Utilising the shape of an organ in the recognition process is accomplished by the use of the morphologic operation called an opening. An opening is essentially a shape filter where organ objects are eliminated which do not meet a particular shape criteria. The recognition process uses the spatial relationships between organs to locate the region of one organ based on the location of others. Regions are determined by the use of a morphologic dilation/translation, followed by a logical intersection. A morphologic dilation expands an object based on a particular shape criteria. Shape criteria for morphologic operations are encoded into structuring elements. Structuring elements are simply images where the foreground pixels provide spatial definition. In 3D mathematical morphology the structuring elements are volume images, thus providing for 3D spatial definitions. The definitions of the basic morphological operations can be found in the tutorial by Haralick et. al. [11].

The basic scheme in using 3D mathematical morphology for the identification of an organ is to determine a gross search volume. Initially, a general location relationship is used; such as the eyes are located near the axial midplane of the head. Then as more organs are found, the relative location of the search volume can be narrowed by the relationship of the goal organ to those organs already found. The search volume for the goal organ is converted from a greyscale to a binary image. For organs that have a strong contrast between them and adjacent structures, the binarization involves just a single thresholding step. For organs in which the contrast between them and adjacent structure is more subtle, additional greyscale morphology preprocessing may be required prior to the thresholding. Then the objects in the search space which do not meet the basic shape criteria for the goal organ are filtered out. In general, once the basic shape of the organ is found, the search volume is reduced. A less restrictive shape criteria is then used to find the finer detail of the goal organ within this reduced search volume.

2 COMPUTATIONAL CONSIDERATIONS

Morphologic operations can be computationally intensive, especially when operating on 3D image volumes. In the area of robotic computer vision, real-time systems have been developed. Real time refers to performing an operation in a time period on the order of a video signal frame rate, usually 30 or 60Hz. As computer vision systems are geared toward video signals, morphologic operations are implemented for 2D images. In order to utilize a computer vision system, it is necessary to decompose the 3D morphologic operations into a series of 2D operations.

In order to decompose the 3D mathematical morphology primitive operations into 2D operations, the following morphologic properties, developed by proof in [11], will be needed.

$$A \ominus B = \bigcap_{b \in B} A_{-b} \tag{1}$$

$$A \ominus (B \cup C) = (A \ominus B) \cap (A \ominus C) \tag{2}$$

$$(A \ominus C) \cup (B \ominus C) \subseteq (A \cup B) \ominus C \tag{3}$$

$$A \oplus (B \cup C) = (A \oplus B) \cup (A \oplus C) \tag{4}$$

$$(A \cup B) \oplus C = (A \oplus C) \cup (B \oplus C) \tag{5}$$

The following definitions will provide the constraints under which four additional morphologic properties will be derived by proof.

Definition 1 *Let Ω be the universal set in Euclidean 3-space with parallel planar partitions, denoted by $\{\ldots, \Omega_{-1}, \ldots, \Omega_0, \ldots$ and having the following properties:*

$$\Omega = \bigcup_{i=-\infty}^{\infty} \Omega_i \quad \text{where} \quad \Omega_i \cap \Omega_j = \emptyset \quad \text{for all} \quad i \neq j \tag{6}$$

$$\text{if} \quad a \in \Omega_m \quad \text{and} \quad b \in \Omega_n \quad \text{then} \quad a + b \in \Omega_{m+n} \tag{7}$$

Definition 2 *Let A be any 3D set, then its 2D parallel planar subsets, A_i, can be defined as*

$$A_i = A \cap \Omega_i \tag{8}$$

Hence,

$$A = \bigcup_{i=-\infty}^{\infty} A_i \quad \text{where} \quad A_i \cap A_j = \emptyset \quad \text{for all} \quad i \neq j \tag{9}$$

Property 1 *Given two 2D sets, $A_m \in \Omega_m$ and $B_n \in \Omega_n$, each being a parallel planar partition as defined in Equation 8, then*

$$A_m \ominus B_n \subseteq \Omega_{m-n} \tag{10}$$

Proof 1 *Let $c \in (A_m \ominus B_n)$. Then for every $b \in B_n$, $c+b \in A_m$. But $c+b \in A_m$ implies $c \in (A_m)_{-b}$. Now, since $A_m \subseteq \Omega_m$, and $B_n \subseteq \Omega_n$, then $(A_m)_{-b} \subseteq (\Omega_m)_{-b} = \Omega_{m-n}$.*

Property 2 *Given two 2D sets, $A_m \in \Omega_m$ and $B_n \in \Omega_n$, each being a parallel planar partition as defined in Equation 8, then*

$$A_m \oplus B_n \subseteq \Omega_{m+n} \tag{11}$$

Proof 2 *Let $c \in (A_m \oplus B_n)$. Then for some $a \in A_m$ and $b \in B_n$, $c = a+b$, which implies $c \in (A_m)_b$. Now, since $A_m \subseteq \Omega_m$, and $B_n \subseteq \Omega_n$, then $(A_m)_b \subseteq (\Omega_m)_b = \Omega_{m+n}$.*

Property 3 *Given three parallel planar sets, $A_i \subseteq \Omega_i$, $B \subseteq \Omega_j$, and $C \subseteq \Omega_k$, with $i \neq j$.*

$$\text{if } C \subseteq (A \cup B), \text{ then } C \subseteq A \text{ and } C \subseteq B \tag{12}$$

Proof 3 *Suppose $C \subseteq (A \cup B)$ and suppose it is not the case that $C \subseteq A$ and $C \subseteq B$. Then there exists an $x, y \in C$ such that $x \in A$ and $y \in B$. But $x, y \in C$ implies $x, y \in \Omega_k$, while $x \in A$ implies $x \in \Omega_i$ and $y \in B$ implies $y \in \Omega_j$. Now $x \in (\Omega_i \cap \Omega_k)$ implies $k = i$ and $y \in (\Omega_j \cap \Omega_k)$ implies $k = j$. But $k = i$ and $k = j$ implies $i = j$, which is a contradiction. Therefore the supposition that it is not the case that $C \subseteq A$ and $C \subseteq B$ is false, and it must be the case that $C \subseteq A$ and $C \subseteq B$.*

Property 4 *Given three parallel planar sets, $A \subseteq \Omega_i$, $B \subseteq \Omega_j$, and $C \subseteq \Omega_k$, with $i \neq j$, then*

$$(A \cup B) \ominus C = (A \ominus C) \cup (B \ominus C) \tag{13}$$

Proof 4 *By Equation 3, it is alway the case that $(A \ominus C) \cup (B \ominus C) \subseteq (A \cup B) \ominus C$, so we only have to prove $(A \cup B) \ominus C = (A \ominus C) \cup (B \ominus C)$. Let $x \in (A \cup B) \ominus C$ then $C_x \in (A \cup B)$. Since $C \in \Omega_k$, there exists a m, such that $C_x \in \Omega_m$. Now, $A \in \Omega_i$, $B \subseteq \Omega_j$, and $C_x \subseteq \Omega_m$, with $i \neq j$, implies $C_x \subseteq A$ or $C_x \subseteq B$. But, $C_x \subseteq A$ implies $x \in (A \ominus C)$, and $C_x \subseteq B$ implies $x \in (B \ominus C)$. Hence, by Equation 12, $x \in (A \ominus C) \cup (B \ominus C)$.*

2.1 3D Erosion

Consider a 3D erosion of a set A, by a structuring element K, both of which are partitioned into parallel planar subsets according to Equation 8.

$$A \ominus K = \left[\bigcup_{m=-\infty}^{\infty} A_m \right] \ominus \left[\bigcup_{n=-\infty}^{\infty} K_n \right] \tag{14}$$

Using the property of Equation 2, the erosion by a union in Equation 14 is equal to an intersection of erosions.

$$A \ominus K = \bigcap_{n=-\infty}^{\infty} \left[\bigcup_{m=-\infty}^{\infty} A_m \right] \ominus K_n \tag{15}$$

Using Property 4 of Equation 13, the erosion of a union is equal to a union of erosions.

$$A \ominus K = \bigcap_{n=-\infty}^{\infty} \bigcup_{m=-\infty}^{\infty} (A_m \ominus K_n) \tag{16}$$

Since the result of an erosion is a set, it can be partitioned into parallel planar subsets by Equation 8.

$$(A \ominus K) \cap \Omega_i = \left[\bigcap_{n=-\infty}^{\infty} \bigcup_{m=-\infty}^{\infty} (A_m \ominus K_n) \right] \cap \Omega_i \tag{17}$$

Now, by the distributive property of intersections over unions

$$(A \ominus K) \cap \Omega_i = \bigcap_{n=-\infty}^{\infty} \bigcup_{m=-\infty}^{\infty} ((A_m \ominus K_n) \cap \Omega_i) \tag{18}$$

But $(A_m \ominus K_n) \subseteq \Omega_{m-n}$ by Property 1 of Equation 10, so that

$$(A_m \ominus K_n) \cap \Omega_i = \begin{cases} \emptyset, & m-n \neq i \\ A_{i+n} \ominus K_n, & m-n = i \end{cases} \tag{19}$$

Then

$$(A \ominus K) \cap \Omega_i = \bigcap_{n=-\infty}^{\infty} (A_{i+n} \ominus K_n) \tag{20}$$

Finally, the 3D erosion for the entire volume is

$$(A \ominus K) = \bigcup_{i=-\infty}^{\infty} [(A \ominus K) \cap \Omega_i] = \bigcup_{i=-\infty}^{\infty} \bigcap_{n=-\infty}^{\infty} (A_{i+n} \ominus K_n) \tag{21}$$

2.2 3D Dilation

Consider a 3D dilation of a set A, by a structuring element K, both of which are partitioned into parallel planar subsets according to Equation 8.

$$A \oplus K = \left[\bigcup_{m=-\infty}^{\infty} A_m \right] \oplus \left[\bigcup_{n=-\infty}^{\infty} K_n \right] \tag{22}$$

Using the property of Equation 4, the dilation by a union in Equation 22 is equal to an union of dilations.

$$A \oplus K = \bigcup_{n=-\infty}^{\infty} \left[\bigcup_{m=-\infty}^{\infty} A_m \right] \oplus K_n \tag{23}$$

Using the property of Equation 5, the dilation of a union is equal to a union of dilations.

$$A \oplus K = \bigcup_{n=-\infty}^{\infty} \bigcup_{m=-\infty}^{\infty} (A_m \oplus K_n) \tag{24}$$

Since the result of an dilation is a set, it can be partitioned into parallel planar subsets by Equation 8.

$$(A \oplus K) \cap \Omega_i = \left[\bigcup_{n=-\infty}^{\infty} \bigcup_{m=-\infty}^{\infty} (A_m \oplus K_n) \right] \cap \Omega_i \tag{25}$$

Now, by the distributive property of intersections over unions

$$(A \oplus K) \cap \Omega_i = \bigcup_{n=-\infty}^{\infty} \bigcup_{m=-\infty}^{\infty} ((A_m \oplus K_n) \cap \Omega_i) \tag{26}$$

But $(A_m \oplus K_n) \subseteq \Omega_{m+n}$ by Property 2 of Equation 11, so that

$$(A_m \oplus K_n) \cap \Omega_i = \begin{cases} \emptyset, & m+n \neq i \\ A_{i-n} \oplus K_n, & m+n = i \end{cases} \tag{27}$$

Then

$$(A \oplus K) \cap \Omega_i = \bigcup_{n=-\infty}^{\infty} (A_{i-n} \oplus K_n) \tag{28}$$

Finally, the 3D dilation for the entire volume is

$$(A \oplus K) = \bigcup_{i=-\infty}^{\infty} [(A \oplus K) \cap \Omega_i] = \bigcup_{i=-\infty}^{\infty} \bigcup_{n=-\infty}^{\infty} (A_{i-n} \oplus K_n) \tag{29}$$

3 APPROACH

The approach taken in this investigation is to first consider a mathematical model of the organ recognition process as described in section 3.1. A partial implementation of the model is then demonstrated by use of a description to algorithm translation as described in section 3.2. As a research starting point, the model has limited use of greyscale mathematical morphology, relying more on binary mathematical morphology, which is less computationally expensive. Thus, the medical images must be converted from greyscale to binary.

3.1 Prototype Theoretical Model

One of the strengths of mathematical morphology is its solid mathematical basis. In order to explore its use in organ recognition, a mathematical model is proposed to guide the development of its implementation. The model uses biological prototypes which consists of a spatial and greyscale extent, and their relationships to each other. A volume image of a biological body, V, consisting of all biological structures in a Z^3 space, is a spatial domain mapping to a greyscale range ($V : Z^3 \rightarrow G$). For each class of biological structure P_n, within V, there exists a set of possible prototypes, p_n, which are a mapping of a spatial sub-domain to a greyscale range, $p_n : D_n \rightarrow G_n$, so that

$$P_n = \{p \mid \ p \textit{ is a prototype for class } n \ \} \tag{30}$$

An oversimplistic example of a prototype for an orbit is $p_{orbits} : sphere(5mm) \rightarrow 40$. Given some translation, t_n, the union of a complete set of prototypes from the same V, will then fill Z^3,

$$\bigcup_{n=1}^{N} (D_n)_{t_n} = Z^3 \tag{31}$$

For example, $(D_{orbits})_{t_{orbits}} \cup (D_{spine})_{t_{spine}} \cup (D_{pons})_{t_{pons}} \cup \ldots \cup (D_N)_{t_N} = Z^3$

The prototypes within a class have relative properties of shape, greyscale range and spatial relationships to prototypes in the other classes. An example of a relative shape relationship is that the orbits are open with respect to a sphere of a radius equal to $\frac{1}{4}th$ the axial radius of spine, $D_{orbits} \circ sphere\left(\frac{R_{spine_z}}{4}\right) = D_{orbits}$. An example of a

relative greyscale property is that the average greyscale value of the spine is greater than the average greyscale value of the orbits, $\bar{G}_{spine} > \bar{G}_{orbits}$. An example of a relative spatial relationship property is that the spine is located below the orbits $t_{spine_z} < t_{orbits_z}$.

Using this model, a decomposition of a volume image into different biological structures can be accomplished by selecting a volume subset based on greyscale range properties, followed by reduction using spatial relationship and shape properties. The greyscale range used for selection of a volume subset for a particular biological structure is made such that there exists a translation of its prototype spatial domain which is contained in the selection

$$S_n = \{v \in Z^3 | \theta_1 < V(v) < \theta_2\} \tag{32}$$

where θ_1 and θ_2 are chosen such that for some translation, q_n, $(D_n)_{q_n} \in S_n$. In the case where the greyscale range overlaps between some prototypes of adjacent biological structures, a single threshold value for all prototypes will not exist that is sufficient to allow subsequent isolation by shape and spatial properties. A more robust method is then required which utilizes the relative greyscale range property between the adjacent structures.

For example, if the average greyscale ranges of the adjacent structures, p_1 and p_2, has the relation $\bar{G}_1 > \bar{G}_2$, and p_1 is surrounded spatially by p_2, then an opening residue can be used. An appropriate structuring element, K, and threshold value, T, must be determined based on the shape and greyscale properties of p_1 and p_2.

$$G_{union} = G_1 \cup G_2 \tag{33}$$

$$G_{open} = G_{union} - (G_{union} \circ K) \tag{34}$$

$$S_n = G_{open} > \frac{\bar{G}_{open}}{T} \tag{35}$$

The selected volume subset, S_n, can be reduced to the biological structure, p_n, by intersecting it with other biological structures, p_m, which have been already found and have been opened, dilated and translated.

$$p_n = \bigcup_{m=1}^{M} S_n \cap [(p_m \circ K_{1_{mn}}) \oplus K_{2_{mn}}]_{x_{mn}} \tag{36}$$

It is necessary to find for each p_m, the minimal structuring elements, $K_{1_{mn}}$ and $K_{2_{mn}}$, which for an appropriate translation, x_{mn}, will satisfy the relation

$$p_n = p_n \cap [(p_m \circ K_{1_{mn}}) \oplus K_{2_{mn}}]_{x_{mn}} \tag{37}$$

3.2 Description to Algorithm Translation

The algorithms used to extract organs in this work are developed based on a method of description translation. Although this method is somewhat ad hoc, the algorithms are consistent with the proposed prototype model. An automated process to select the morphologic structuring elements could be developed given an appropriate description of each organ. In the discipline of Gross Anatomy, organs are described by their shape and relative position. In a straightforward manner, terminology used in these descriptions can be translated into morphologic algorithms. The description of an organ can be used as an object class criteria. The objects in a particular class can be isolated by filtering out those objects that do not meet the shape criteria of that class. The filtering is accomplished by a morphologic opening with the criteria encoded into the structuring element. The encoding is simply a translation of the shape description into an image of that shape.

A model part having a minimum width can be detected by opening the binary image with a horizontal line segment of this minimum width.

$$I_1 = I_0 \circ Horz\_Line(min\_width) \tag{38}$$

Such an opening might select other object parts as well. Indeed all sections of objects which have a horizontal width greater than the length of the horizontal line segment would be selected. Only if the horizontal width was a distinguishing feature would the opening only select the part. Distinguishing feature in this case would mean that no pixel of any other object is in a horizontal extent of length *min_width*. A part having a maximum width can be selected by the complement of the opening intersected with the original image.

$$I_2 = I_0 - (I_0 \circ Horiz\_Line(max\_width)) \tag{39}$$

The intersection of these two operations can be used for a part description distinguished by a width range.

$$I_3 = I_1 \cap I_2 \tag{40}$$

Similarly, for a part criteria of height, the same operations would be used, but with a vertical line as the structuring element. A class criteria that involves both a width and height component simultaneously, is done by combining both dimensions into a single structuring element. The combination is accomplished by a dilation, specifically dilation of the horizontal line by the vertical line, which results in a rectangle.

$$\begin{aligned} I_3 &= Horz\_Line(width) \oplus Vert\_Line(height) && (41)\\ &= rectangle(width, height) && (42) \end{aligned}$$

The combination of two 1D structuring elements of lines into a single 2D structuring element of a rectangle can be extended again to generate a 3D structuring element. For a part criteria that has a given minimum length, width, and height, a rectangular parallelepiped can be used.

$$\begin{aligned} I_5 &= Line(x, 0, 0) \oplus Line(0, y, 0) \oplus Line(0, 0, z) && (43)\\ &= parallelepiped(x, y, z) && (44) \end{aligned}$$

Structuring elements are not restricted to those made up of linear segments, for any shape can be used. For a class criteria of minimum diameter at all 2D angles, a disc can be used, while for 3D, a sphere would be used. For objects that have a minimum diameter in 2D and a minimum extent in a third, the dilation of a disc by the extent would be used, namely a cylinder. For a less restrictive criteria which specifies the part to be of a minimum length in any of one or more directions, a generalized opening can be used. The generalized opening is the union of all the individual openings using the same structuring element, but which have been rotated at different angles. For example, if the part criteria is for a minimum diameter in any 2D multiple of 45 degree direction, the form of the generalized opening would be as follows.

$$I_6 = \bigcup_{\theta \in (0,45,90,135)} I_0 \circ Rotate(Line(min\_diam), \theta) \tag{45}$$

The known spatial relationship between two parts can be used in locating one part based on the location of the other part. The detection algorithm for the second part can be expressed morphologically in three steps. The first step is to dilate the detected first part to account for the distance uncertainty and to account for the size difference in the parts. The second step is to translate the dilated first part so that its center covers the second part. This translation would be the difference in translation of each part's center from the origin of the model coordinate reference frame. The third step is to intersect the translated dilated first part to detect the second part. As an example, consider two disks, R_1 and R_2, of known diameters, r_1 and r_2, $r_1 > r_2$, which are separated by a distance $D \pm d$. Given an image, I_{R2}, of the just isolated first disk and an image, I_B, of both disks, the region of the second disk, I_{R1} can be found as follows:

$$I_{R_1} = I_B \cap (I_{R2} \oplus disk(d + r_1 - r_2))_D \tag{46}$$

4 ORGAN RECOGNITION EXPERIMENTS

For organ recognition experiments given here for the orbits and ventricles, a mathematical description of the spatial relationship, greyscale and shape properties of the organ class is given. As a caveat, these properties were determined based on only one data set. However, an attempt was made to keep the properties general enough so that they would

be valid for all normal MRI data sets of the human head. The image volume used in these experiments was provided by the Mayo Clinic, as part of their Analyze software package [12]. Based on these description, the reasoning behind the translation of these properties into a recognition algorithm is then discussed. The recognition algorithm is implemented by a series of morphologic procedures. For selected morphologic steps in the procedures, an axial slice image mosaic showing the results is given.

4.1 Orbit Recognition

4.1.1 Orbit Spatial Relationship Properties

1. The orbits can be located in a region which contains the the axial midplane, Z_{mid}, and has an axial height equal to 30% of the height of the head, dZ_{head}. The region is extends below Z_{mid} by 10% of dZ_{head} and above Z_{mid} by 20% of the head dZ_{head}. (See Figure 2a).

$$max(orbits_z) < Z_{hi} = Z_{mid} + \frac{dZ_{head}}{5} \tag{47}$$

$$min(orbits_z) > Z_{lo} = Z_{mid} - \frac{dZ_{head}}{10} \tag{48}$$

2. As shown in Figure 2b, an initial search volume, D_{isv}, which contains the orbits can be defined as:

$$D_{orbits} \subset D_{isv} = \{d \mid d(x,y,z) \in Z^3 \quad where \quad Z_{lo} \leq z \leq Z_{hi}\} \tag{49}$$

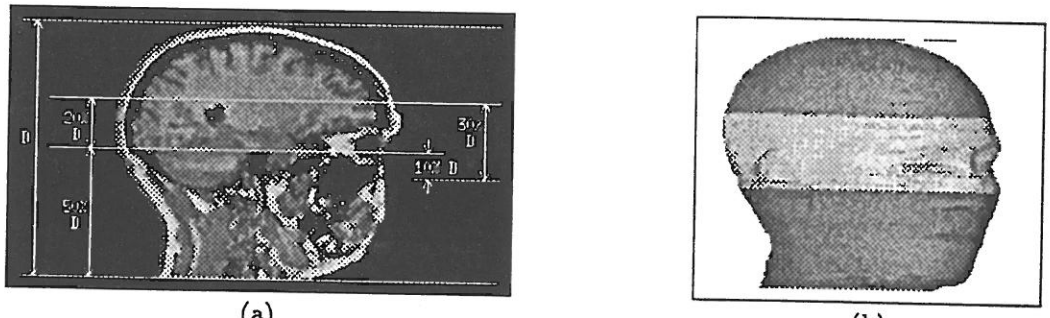

(a) (b)

Figure 2: Orbit initial search volume.

4.1.2 Orbit Greyscale Properties

1. The average greyscale value of the orbits, $\bar{G}_{orbits}$, are relatively darker than the average greyscale value of the surrounding region, $\bar{G}_{sr}$. The surrounding region is obtained by dilation of the orbits by a sphere, K_{s1}, of radius equal to $\frac{1}{3}rd$ the maximum orbit radius.

$$G_{orbits} = G_{head} \cap D_{orbits} \tag{50}$$

$$G_{sr} = G_{head} \cap [\overline{D_{orbits}} \cap (D_{orbits} \oplus K_{s1})] \tag{51}$$

$$\bar{G}_{orbits} < \bar{G}_{sr} \tag{52}$$

2. A subset, D_{ss1}, of the initial search volume, D_{isv}, which is still a superset of the orbits, D_{orbits}, can be obtained by thresholding a closing residue, G_{cr}. The closing is with an axial disk structuring element, K_d, of radius equal to 20% of the minimum axial head radius.

$$G_{cr} = (G_{isv} \bullet K_d) - G_{isv} \tag{53}$$

$$D_{ss1} = G_{cr} > \frac{max(G_{cr})}{2} \tag{54}$$

$$D_{orbits} \subset D_{ss1} \subset D_{isv} \tag{55}$$

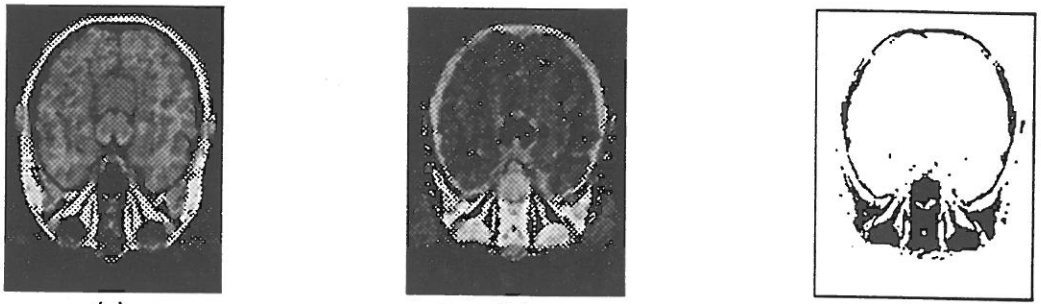

(a) (b) (c)

Figure 3: Orbit binarization by thresholding a closing residue.

4.1.3 Orbit Shape Properties:

1. A subset, D_{ss2}, of the initial search volume, D_{isv}, which is still a superset of the orbits can be obtained by removing objects which are larger than 150% than the diameter of an orbit. A generalized opening with a line structuring element, K_l, is used to find the set of objects, D_{go}, larger than the maximum size for subsequent removal by a logical intersection.

$$D_{go} = \bigcup_{\theta \in (0°, 45°90°, 135°)} D_{isv} \circ rotate(K_l, \theta_z) \tag{56}$$

$$D_{ss2} = D_{isv} \cap \overline{D_{go}} \tag{57}$$

$$D_{orbits} \subset D_{go} \subset D_{isv} \tag{58}$$

2. The orbits are open with respect to a sphere structuring element, K_{s2}, which is 20% of the nominal orbit radius. The nominal orbit size is taken as 15% of the minimum axial head radius.

$$D_{orbit} = D_{orbit} \circ K_{s2} \tag{59}$$

4.1.4 Orbit Algorithm Reasoning

1. Since the orbits are located just above the axial mid-plane of the head, taking the axial planes which lie 10% below the mid-plane, (50% - 10% = 40%), and those 20% above the mid-plane, (50% + 20% = 70%), will insure a region which contains the orbits.

2. The orbits are dark regions with greyscale values in the range of the background values and thus appear as voids. Thresholding the greyscale image below the maximum void value will bring all the void regions to the foreground in the resulting binary image.

3. The regions external of the head are in the same greyscale range as the internal voids, thus the interior of the head needs to be found in order to eliminate the external regions. The internal region is found by first performing a greyscale closing to fill internal voids. There are no voids in the head of diameter greater than 40% the sagittal width of head. So a greyscale closing with a disk structuring element of a diameter equal to 40% the sagittal width of the head is done, followed by thresholding above the the maximum void value.

4. Objects which are substantially larger than the orbits are removed by eliminating void objects which are 150% of the orbit diameter. The diameter of the orbits is approximated as 15% of the minimum width of head.

5. Of the remaining small voids objects, there are none which are spherically larger than 20% of the approximate orbit size, except for the orbits. Since the orbits are not perfect spheres, a spherical structuring element of only 20% of their approximate size is used.

4.1.5 Orbit Morphologic Procedure

1. $G_0 = G_{head} \cap D_0$
   Extract the head region from 40% to 70% of the head axial height. (See Figure 4a, which shows a subset of the image planes from the initial search volume).

2. $B_0 = (G_0 \bullet disc(32)) > 45$
   Find the internal head region.

3. $B_1 = G_0 < 45$
   Find the void regions.

4. $B_2 = B_0 \cap B_1$
   Isolate the internal head voids. (See Figure 4b)

5. $B_3 = B_2 \circ sphere(1)$
   Disconnect trivially touching objects.

6. $B_4 = \bigcup_{\theta \in \{0,45,90,135\}} B_3 \circ rotate(line_x(37), \theta)$
   Perform a generalized opening to find all objects with a dimension greater than 150% of the approximated orbit diameter. (See Figure 4c)

7. $B_5 = B_3 \cap \overline{B_4}$
   Remove objects with dimensions greater than 150% of the orbits. (See Figure 4d)

8. $B_6 = B_5 \circ sphere(5)$
   Remove all objects with a radius greater than 20% of the orbits. (See Figure 4e)

4.2 Ventricle Recognition

4.2.1 Ventricle Spatial Relationship Properties

1. The ventricles are located above the top of the orbits and within half the distance between the top of the orbits and the top of the head. (See Figure 5a).

$$min(ventricles_z) > Z_{lo} = max(orbits_z) \tag{60}$$

$$max(ventricles_z) < Z_{hi} = Z_{lo} + \frac{max(head_z) - Z_{lo}}{2} \tag{61}$$

2. The ventricles are located within a region, D_m, that is located in middle $\frac{2}{3}rds$ of the head axial planes. D_m is obtained by eroding the head volume with an axial plane disk, K_d, of radius $\frac{1}{6}th$ that of the maximum head radius. (See Figure 5b).

$$D_{ventricle} \subset D_m = D_{head} \ominus K_d \tag{62}$$

3. The initial search volume, D_{isv}, for the ventricles is the region within the middle $\frac{2}{3}rds$ of the maximum head radius, D_m, from above the obits, Z_{lo}, up to half way to the top of the head, Z_{hi}. (See Figure 5c).

$$D_{ventricles} \subset D_{isv} = \bigcup_{z=Z_{lo}}^{Z_{hi}} D_m \tag{63}$$

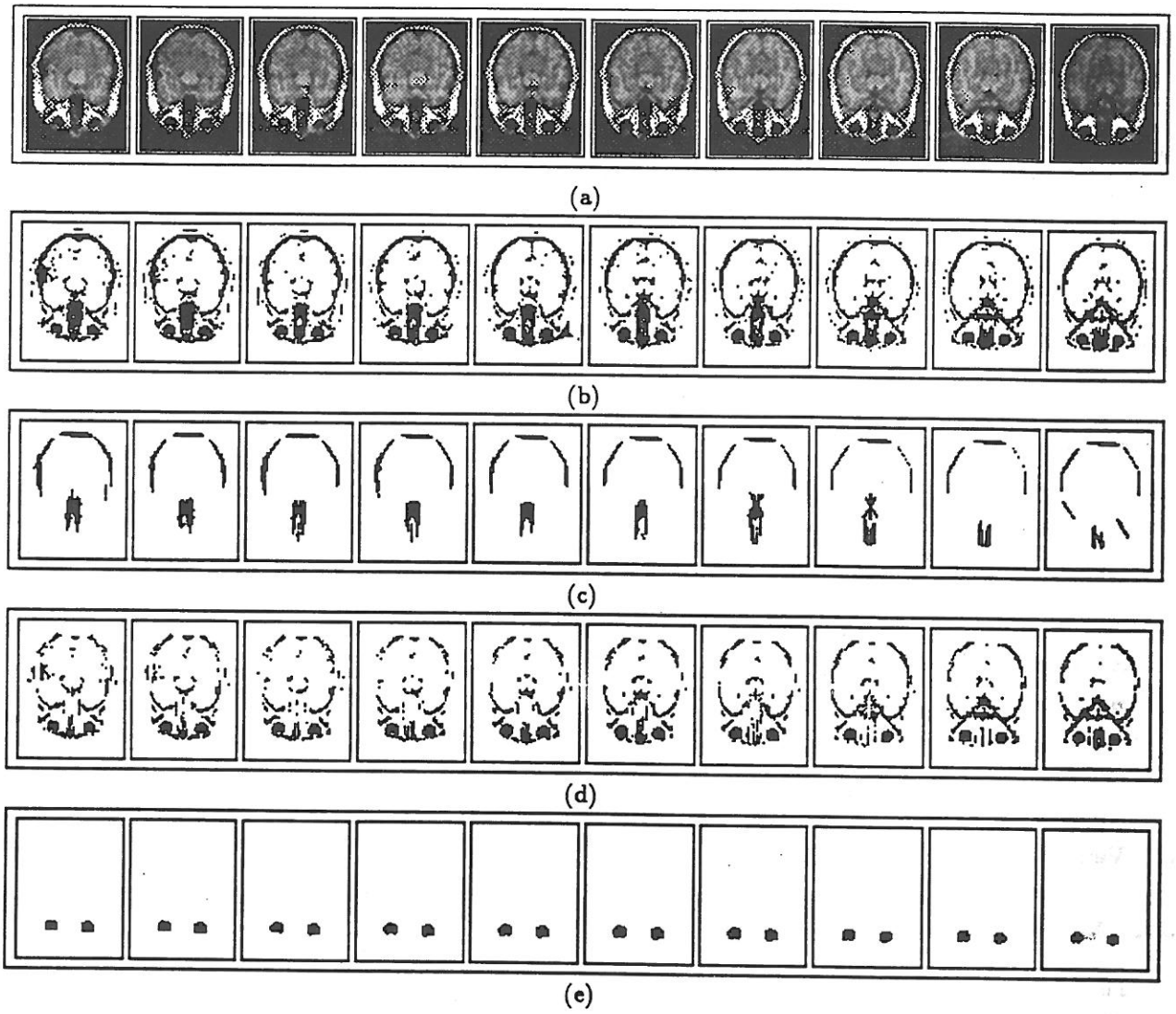

Figure 4: Orbit morphologic processing results.

4.2.2 Ventricle Greyscale Properties

1. The average greyscale value of the ventricles, $\bar{G}_{ventricles}$, are relatively darker than the average greyscale value, $\bar{G}_{sr}$, of the surrounding region in initial search volume, D_{isv}.

$$G_{ventricles} = G_{isv} \cap D_{ventricles} \tag{64}$$

$$G_{sr} = G_{isv} \cap \overline{D_{ventricles}} \tag{65}$$

$$\bar{G}_{ventricles} < \bar{G}_1 \tag{66}$$

2. A subset, D_{ss1}, of the initial search volume, D_{isv}, which is a superset of the ventricles, $D_{ventricles}$, can be obtained by thresholding an opening residue, G_{or}. The structuring element, K_l, is a sagittally directed line of length equal to half the sagittal length of the initial search volume. The thresholding value is half the maximum value of the opening residue, G_{or}. (See Figure 6)

$$G_{or} = G_{isv} - (G_{isv} \circ K_l) \tag{67}$$

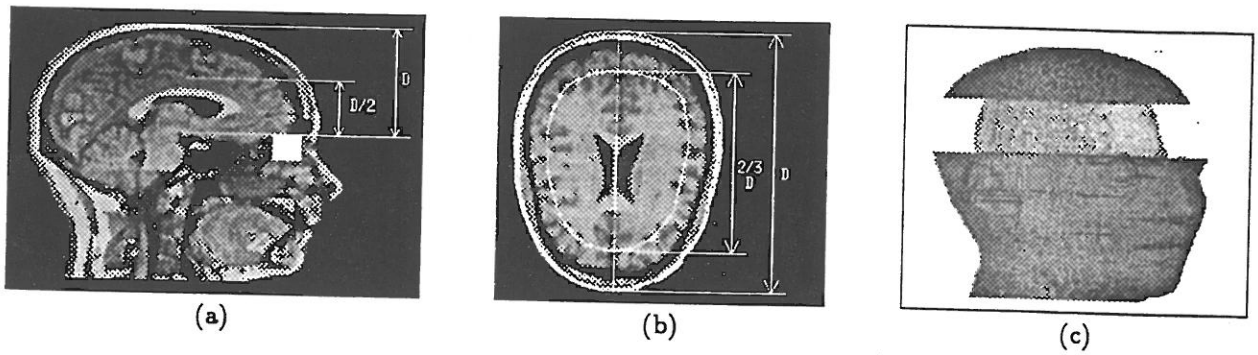

(a) (b) (c)

Figure 5: Ventricle initial search volume.

$$D_{ss1} = G_{or} > \frac{max(G_{or})}{2} \tag{68}$$

$$D_{ventricles} \subset D_{ss1} \subset D_{isv} \tag{69}$$

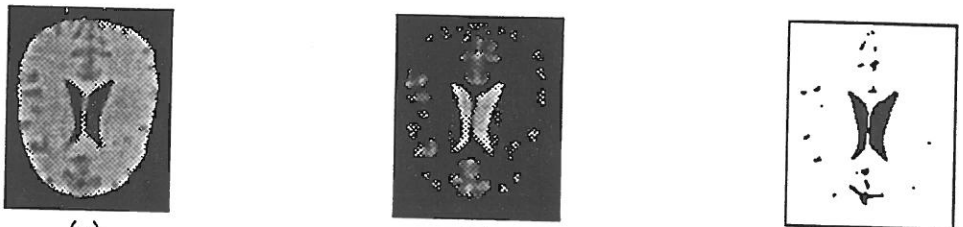

(a) (b) (c)

Figure 6: Ventricle binarization by thresholding a closing residue.

4.2.3 Ventricle Shape Properties

1. The axial height of the ventricles, $dZ_{ventricles}$, is less than the axial height of the orbits, dZ_{orbits}.

$$dZ_{ventricles} < dZ_{orbits}$$

2. The maximum axial radius of the ventricles R_v, from the centroid of the ventricles, is less than half the maximum axial radius of the head, R_h, from the centroid of the head.

$$R_v < \frac{R_h}{2}$$

3. A non-empty subset, D_{ss2}, of the ventricles is open with respect to a coronally directed line structuring element, K_{l1}, with length equal to the orbit diameter.

$$D_{ss2} = D_{ventricles} \circ K_{l1} \tag{70}$$

$$D_{ventricles} \supset D_{ss2} \supset \emptyset \tag{71}$$

4. A non-empty subset, D_{ss3}, of the ventricles is open with respect to a set of structuring elements consisting of a $-45°$, $0°$ and $45°$, rotated coronally directed line structuring elements, K_{l2}, of length equal to the orbit radius.

$$D_{ss3} = \bigcup_{\theta \in (-45°, 0°, 45°)} D_{ventricles} \circ rotate(K_{l2}, \theta r_x) \tag{72}$$

$$D_{ventricles} \supset D_{ss3} \supset \emptyset \tag{73}$$

4.2.4 Ventricle Algorithm Reasoning

1. Since the ventricles are located above the orbits and half way to the top of the head, taking those planes will insure a region that contains the ventricles.
2. Generation of a head interior mask is accomplished by closing all the interior voids.
3. The interior head voids are found by subtracting the thresholded image from the head interior mask.
4. The middle $\frac{2}{3}rds$ of the head can be determined by eroding the interior head mask by a disc of radius $\frac{1}{3}rd$ the diameter of the head.
5. The main body of the ventricles can be extracted by an opening with a coronally directed cylinder structuring element.
6. The search volume can be reduced to a region about the main body. The reduce volume is generated by dilating the main body to a size equal to half the head diameter.
7. A crude extraction of the lobes and main body of the ventricles can be accomplished by a generalized opening, using a line structuring element in the axial plane which is rotated $0°$, $-45°$ and $+45°$.
8. The finer detail of the ventricles can be extracted by first, dilating the crude extraction to form a mask, and then intersecting the mask with the initial binary image.

4.2.5 Ventricle Morphologic Procedure

1. $G_0 = G_{head} \cap D_0$
   Extract the head region from above the orbits and half way to the top of the head. (See Figure 7a, which shows a subset of the image planes from the initial search volume).
2. $B_0 = G_0 > 50$
   Binarization to separate voids from T1 responsive tissues.
3. $B_1 = B_0 \bullet \mathit{disc}(12)$
   Fill in the voids that are of radius 12 or less in the axial plane.
4. $B_2 = B_1 - B_0$
   Take the residue of the closing to extract candidate interior voids.
5. $B_3 = B_1 \ominus \mathit{disc}(30)$
   Generate mask of the middle two-thirds of the head interior.
6. $B_4 = B_3 \cap B_2$
   Extract voids from the middle two-thirds of the head interior. (see Figure 7b)
7. $B_5 = B_4 \circ \mathit{cylinder}(1, 20)$
   Locate the trunk of the ventricles with a long coronal tube. (see Figure 7c)
8. $B_6 = B_5 \oplus (\mathit{line}_x(10) \oplus \mathit{line}_y(54) \oplus \mathit{line}_z(50))$ Generate a mask centered on the trunk of the ventricles. The mask is half the size of the head axial plane dimensions and is equal to the axial height of the orbits. (see Figure 7d)
9. $B_7 = B_4 \cap B_6$
   Locate the region that is centered on the ventricles which is half the size of the head axial plane dimensions and equal to the axial height of the orbits. (see Figure 7e)
10. $B_8 = \bigcup_{\theta \in (-45°, 0°, 45°)} B_7 \circ \mathit{rotate}_z(\mathit{line}_y(10), \theta)$ Extract the branches of the ventricles by a generalize opening. (see Figure 7f)

5 CONCLUSION

The use of 3D mathematical morphology has been shown to be a promising approach to fully automated organ recognition. The preliminary mathematical model is limited in its use of a nominal threshold range for tissue classification. Incorporation of the greyscale morphology preprocessing and/or different tissue classification strategies would make the process more robust. Implementation of a full scale system would require a substantial effort in determining all of the appropriate structuring elements and processing steps. However, given a fully developed mathematical model and a complete 3D sample anatomic atlas, these parameters have the potential for automated determination.

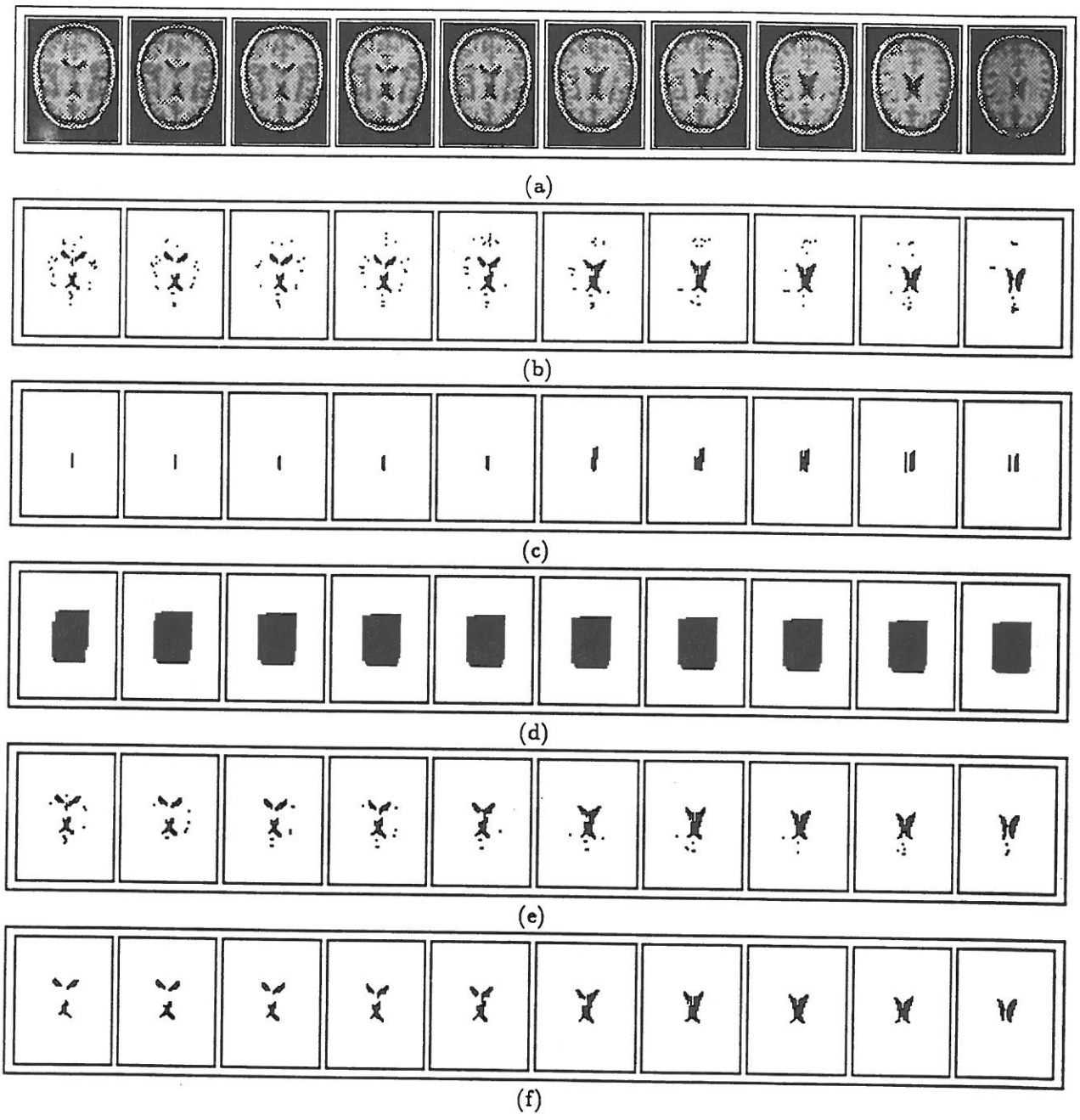

Figure 7: Ventricle morphologic processing results.

References

[1] J. Brinkley. Semi-automatic medical image segmentation using knowledge of anatomic shape. *Medical Imaging V*, 1445:78–87, 1991.

[2] D. Kennedy, P. Filipek, and V. Caviness. Anatomic segmentation and volumetric calculations in nuclear magnetic resonance imaging. *IEEE Trans. on Medical Imaging*, 8(1):1–7, 1989.

[3] J. Ezrielev and S. Dzik. An image editor for 3D-CT reconstruction. *Medical Imaging IV: Image Processing*, SPIE 1233:67–76, 1990.

[4] A. Dhawan and S. Juvvadi. Knowledge-based analysis and understanding of 3D medical imaging. *Medical Imaging II: Image Data Managemament and Display*, SPIE 914:422–428, 1988.

[5] J. Winter. Automated computer tomography image analysis using contour map topology. *IEEE Trans. on Medical Imaging*, MI-3(4):163–169, 1984.

[6] Greenshields I. and K. Yoon. Projecting MRI data into parametric surfaces. *Medical Imaging III: Image Processing*, SPIE 1092:54–59, 1989.

[7] L. Andrews, J. Klingler, J. Schindler, M. Begeman, M. Habboub, D. Farron, B. Vaughan, B. Roggs, and J. Cestaro. Application of mathematical morphology for detection and interconnectivity analysis of porosity in aluminum castings for industrial CT scans. *Proc. American Society for Non-Destructive Testing: Industrial Computed Tomography II*, pages 148–152, 1991.

[8] M. Bomans, K. Hohne, U. Tiede, and M. Riemer. 3-D segmentation of MR images of the head for 3-D display. *IEEE Trans. on Medical Imaging*, 9(2):177–183, 1990.

[9] A. Vepsalainen. Extraction of fibre like objects from 3D images of cells. *Image Algebra amd Morphological Image Processing*, SPIE 1350:201–208, 1990.

[10] F. Preteux, B. Laval-Jeantet, and M. Laval-Jeantet. New prospects in CT image processing via mathematical morphology. *Europ. J. Radiology*, 5:313–317, 1985.

[11] R. Haralick, S. Sternberg, and X. Zhuang. Image analysis using mathematical morphology. *IEEE Trans. on Pattern Analysis and Machine Intelligence*, PAMI-9(4):532–550, 1987.

[12] Biotechnology Computer Resource, Mayo Foundation, Rochester, MN. *Analyze User's Manual*, version 4.0 edition, 1990.